Space-time Galerkin methods for simulation of laser heating using the generalized nonlinear model

M.F. Wakeni[a,b,c,*], B.D. Reddy[a,b]

[a] *Centre for Research in Computational and Applied Mechanics (CERECAM), University of Cape Town, Rondebosch 7701, South Africa*

[b] *Department of Mathematics and Applied Mathematics, University of Cape Town, Rondebosch 7701, South Africa*

[c] *Division of Infrastructure and Engineering, University of Glasgow, United Kingdom*

Abstract

The generalized thermal model is a thermodynamically consistent extension of the classical Fourier's law for describing thermal energy transportation which is very relevant to applications involving very small length, time scales and/or at extremely low temperatures. Under such conditions, thermal propagation has been observed to manifest as waves, a phenomena widely referred to as second sound effect. However, this is in contrast to the paradoxical prediction of the Fourier's model that thermal disturbances propagate with infinite speed. In this work, we review the nonlinear model based on the theory of Green and Naghdi for thermal conduction in rigid bodies and present its implementation within a class of space-time methods. The unconditional stability of the time-discontinuous Galerkin method without restriction over the grid structure of the space-time domain is proved. We also perform a number of numerical experiments to study the convergence properties and analyze the thermal response of materials under short-pulsed laser heating in two space dimensions.

Keywords: Generalized thermal model, Fourier's law, second sound, time-discontinuous Galerkin method, short-pulsed laser

*Corresponding author

Email addresses: mebratu.wakeni@uct.ac.za (M.F. Wakeni), daya.reddy@uct.ac.za (B.D. Reddy)

1. Introduction

Research activity in the development and improvement of existing laser technology has witnessed significant growth over the last decades. This is due to its increased application in fields including engineering material science, medical sciences as well as in the military. For instance, in microelectronic and optoelectronic applications, short-pulsed lasers are used to process thin films [1, 2]; also, in metallurgy, lasers can provide selective treatment of metal surfaces for hardening. In such context, it is important to understand the models for thermal energy transmission in the system. Interestingly, the classical Fourier's law for heat conduction has remarkably held on for well over a century in validating heat conduction experiments, showing significant success in a broad range of engineering and scientific applications. However, as the involved time and length scales decrease, say as a result of the recent trend to miniaturization of devices for application in micro and nano-technology, certain effects previously unaccounted for become prevalent, such that descriptions under the classical (macroscopic) continuum theories like the Fourier's law become insufficient [3].

Theoretical discovery of the physical impossibility of instantaneous transmission of thermal energy disturbances as predicted by the parabolic Fourier's model of heat conduction led scientists to conjecture a wave-like transport of thermal energy [4], thereby suggesting the possibility of the existence of thermal waves in super-fluids in certain temperature regimes [5–7]. Further, thermal waves (the so-called *second sound*) had been observed experimentally in super-fluids and pure crystalline solids [8–12]. The reader is referred to [13–17] for detailed review of the literature on the experimental and theoretical basis for non-Fourier heat conduction.

Motivated by the perceived drawbacks of the classical model for thermal conduction, various modifications of Fourier's theory have been proposed. The first attempts in formulating theories accounting for propagation of thermal waves at finite speed were due to Cattaneo [18], Vernotte [19] and Maxwell [20]. The introduction of a relaxation time to modify Fourier's law results in an equation of damped hyperbolic-type which supports a wave-like mechanism for thermal transport. This model is commonly referred to as the

Cattaneo–Vernotte–Maxwell equation: see [21], for example. For much of the historical development and theoretical justifications of the Cattaneo–Vernotte–Maxwell equation, see the review articles [16, 17, 22, 23, 23–25]. Although the Cattaneo-Vernotte-Maxwell model has been used extensively in modelling wave-like thermal propagation in various applications [25–29], its validity and derivation have been the subject of considerable debate among researchers [30–32].

This has led to considerable attention towards a unified formulation of a widely valid thermal conduction theory with a broader validity than the classical Fourier's law, and consistent with the statistical physics as well as the laws of thermodynamics [3, 32–34]. In the 1990s Green and Naghdi [35–39] proposed a unified thermoelastic framework capable of reproducing the second sound phenomenon. In their approach, a time primitive for the absolute temperature, referred to as *thermal displacement* analogous to material displacement in the theory of deformable bodies, was introduced into the thermodynamic state variables. This formulation subsequently attracted a significant research audience: see, for example, [40–44] and the references therein. Recently, in [51], we extended their model of thermoelasticity into a fully-nonlinear thermal regime in a thermodynamically consistent manner. The extension coupled the nonlinear hyperbolic heat condition with elasticity at finite strains. Its linearisation about a reference state reduces to the model due to Green and Naghdi.

In the present work, we apply this nonlinear model to study the thermal response of materials under short-pulsed lasers. The materials under consideration are assumed to be rigid so that the effect of deformation on thermal response is neglected. Much of the literature on the numerical modelling of non-Fourier thermal response have been based on the Cattaneo–Vernotte–Maxwell equation. Numerical solution of such models has been achieved using a variety of different techniques. For instance, Ai and Li [1] applied a discontinuous Galerkin (DG) scheme spatially with an explicit temporal integration in one, two and three spatial dimensions to simulate the non-Fourier effect due to short-pulsed laser processing of thin films. In related studies, Miller and Haber [21] proposed a space-time discontinuous method which they referred it to as asynchronous spacetime discontinuous Galerkin (aSDG) method. The aSDG method allows for discontinuities of the temperature and heat flux

fields across boundaries of space-time elements. It is element-wise conservative and employs a causal space-time meshing supporting variable element duration and patch-wise solution schemes with linear computational complexity. It also supports dynamic adaptive meshing. However, the implementation of aSDG adaptivity is difficult due to the challenges of casual meshing. A variety of finite difference and finite volume methods with different slop limiters were used by Sasmal and Mishra [45] for the non-Fourier model that accounts for volumetric radiation heat transfer term in two spatial dimension. Mishra and Sahai [46] employed the lattice Boltzmann method to analysize non-Fourier effects in one dimensional cylindrical and spherical geometries. Zhang et al. [47] used a homogenization technique in conjunction with a conforming mixed finite element method to simulate non-Fourier effects in heterogeneous media. Wang et al. [48] employed finite element/finite difference schemes in one space dimension. Bargmann and Steinmann [49, 50] used Galerkin finite element methods both in space and in time for the thermoelastic coupling based on the non-Fourier theory of Green and Naghdi. Though space and time discretizations were treated with Galerkin finite element methods, we note that their approach is not strictly a space-time approach in the sense of the space-time methods discussed in [51–53, 55, 56].

Traditional methods such as finite difference and conforming finite element tend to generate spurious oscillations when the solutions involve the propagation of steep gradients or discontinuities, unless extra stabilization technique are employed, for example, by adding a tunable 'artificial viscosity' term. The disadvantage of artificial viscosity is that it results in excessive damping which severely limits accuracy. Discontinuous Galerkin methods have received increased attention in recent years due to their superior stability behavior without the need for extra stabilization. Under the umbrella of Discontinuous Galerkin methods, space-time methods with some DG features have been the favourite choice for hyperbolic problems. Hughes and Hulbert [56] and Hulbert and Hughes [55] introduced a space-time Galerkin finite element formulation for second-order hyperbolic problems such as elastodynamics. In their formulation the primary unknowns are allowed to be discontinuous in time across the interfaces of space-time slabs, which are hyper-cylindrical partitions of the space-time domain. And their continuities are enforced weakly in terms of the energy in-

ner product which is closely related to the problem itself. Johnson [52] gave convergence analysis and a priori and a posteriori error estimates for the time-discontinuous Galerkin formulation applied to a generic scalar, linear and second-order hyperbolic problem. Fully discontinuous Galerkin space-time methods in both space and time have been proposed for elastodynamics [57–60] and were also adopted to the Cattaneo–Vernotte–Maxwell equation in [21].

Khalmanova and Costanzo [53] extend the time-discontinuous formulation of Hulbert and Hughes to solve the linear thermo-elasto-dynamic problem. While their formulation led to remarkable convergence and stability properties for both the uncoupled and coupled case, the result however, showed dependency of accuracy on N (i.e., the number of elements layers per slab along the time axis) of the space-time mesh. In an earlier work, Costanzo and Huang [54] presented a one field space-time DG formulation for linear problem and showed unconditional stability regardless of the structure of the space-time mesh in each slab. Recently, in [51], we also extended the Hulbert and Hughes space-time formulation to the coupling of classical elastodynamics with the thermal model due to Green and Naghdi in an operator-splitting based algorithm. Unlike the Hulbert and Hughes time-discontinuous method our formulation employs the L^2-inner product to weakly enforce continuity across the interfaces of space-time slabs. This makes it suitable for a natural extension to nonlinear problems, as the L^2-inner product is independent of the problem being solved.

In this article, we present two methods that belong to the family of space-time Galerkin finite element method for the numerical solution of the nonlinear generalized thermal model due to the formulation in [34]. The first is an extension of the time-discontinuous Galerkin method proposed in [51] to the nonlinear generalized thermal model. The other one is a continuous Galerkin space-time method where the principal unknowns are continuous everywhere in the space-time domain. Continuities across the interfaces of each space-time slab are enforced strongly as Dirichlet boundary conditions. The fully discrete nonlinear algebraic systems resulting from the space-time discretizations are solved using an iterative Newton-Raphson scheme. Tangent matrices for the Newton scheme are computed exactly using tools with an automatic differentiation capability [61]. In comparison to the aSDG

method [21], the present time-discontinuous Galerkin (TDG) method is only slab-wise conservative whereas the continuous Galerkin (cG) method do not have conservation property. As a typical DG based method the algorithmic complexity of TDG method can become increasingly higher as the polynomial order increases. This can be circumvented using dynamic adaptivity keeping the temporal thickness $N = 1$ as much as possible.

The structure of the paper is as follows. A brief review of the governing equations is presented in Sec. 2. Important concepts essential for the analysis of the discrete formulations such as the stability of the continuum model, are also discussed in this section. Basic notations and the space-time formulations are presented in Sec. 3. The time-discontinuous and the continuous space-time Galerkin formulations and their stability analysis are also presented. The convergence properties of the two schemes are compared for the linear case with an exact solution in Sec. 4; the capability of the time-discontinuous formulation in resolving fine features of the solution arising from simulations of thermal response of a rigid body under laser pulses in two spatial dimension is also showcased. Finally, in Sec. 5 concluding remarks are presented.

2. The generalized thermal conductivity problem

In this section, we summarize the generalized model of thermal conduction which was derived based on the theory of Green and Naghdi in [34]. The nonlinear stability of the initial-boundary value problem is analyzed using the energy method. The stability analysis will also serve as the basis for a similar stability proof of the proposed discrete schemes.

2.1. An overview of the model

We consider a system involving a rigid body occupying the bounded domain $\Omega \subset \mathbb{R}^d$ ($d = 1, 2$ or 3) with piecewise smooth boundary $\Gamma = \partial\Omega$ subject to a volumetric heat supply $r : \Omega \times \mathbf{I} \to \mathbb{R}$, where $\mathbf{I} = [0,\ T]$ is the time interval of interest. Let the scalar field $\vartheta : \Omega \times \mathbf{I} \to \mathbb{R}$ denote the relative temperature with respect to a uniform reference temperature $\Theta_0 > 0$ such that the absolute temperature is given by $\Theta = \vartheta + \Theta_0 > 0$. The

local balance of energy equation is given by

$$\dot{\varepsilon} = -\mathrm{div}\, \boldsymbol{q} + r, \tag{1}$$

where ε is the volumetric internal energy of the system and $\boldsymbol{q}$ the heat flux vector, and the superposed dot and div indicate the time derivative and the divergence operator, respectively. The generalized theory of thermal conduction is based on the assumption that the heat flux vector $\boldsymbol{q}$ is not entirely dissipative as in the case of Fourier's law. Rather it is composed of two components, the energetic part $\boldsymbol{q}_e$ and the Fourier-like dissipative part $\boldsymbol{q}_d$ such that

$$\boldsymbol{q} = \boldsymbol{q}_e + \boldsymbol{q}_d.$$

In addition to this, the generalized theory also introduces a thermodynamic state variable, the so-called thermal displacement α, which is the primitive of the absolute temperature, that is

$$\alpha = \alpha^0 + \int_{t_0}^{t} \Theta(\cdot, s)\mathrm{d}s. \tag{2}$$

In this work, we assume that the initial thermal displacement α^0 is uniform over the spatial domain. By formally exploiting the argument of the imbalance of entropy (second law of thermodynamics), the rate of net energy production becomes

$$\dot{\varepsilon} - \Theta\dot{\eta} = \Theta^{-1}\boldsymbol{q}_e \cdot \nabla\Theta, \tag{3}$$

where η is the entropy of the system (measured per unit temperature) and ∇ denotes the spatial gradient operator. Combining equations (1) and (3), we obtain

$$\Theta\dot{\eta} = -\mathrm{div}\, \boldsymbol{q} + \Theta^{-1}\boldsymbol{q}_e \cdot \nabla\Theta + r. \tag{4}$$

Thermodynamically consistent constitutive equations that represent a wide range of materials are given by[1]

$$\eta = C \ln[\Theta/\Theta_0] + \xi_0, \tag{5}$$

$$\boldsymbol{q}_e = -\Theta \boldsymbol{k}_1 \nabla\alpha, \tag{6}$$

$$\boldsymbol{q}_d = -\boldsymbol{k}_2 \nabla\Theta, \tag{7}$$

where $C := \rho c$ is the volumetric heat capacity, ρ the mass density, c the specific heat capacity, $\boldsymbol{k}_1$ is a positive-definite non-classical conductivity (which accounts for the time and length scales that are responsible for the second sound effect), and $\boldsymbol{k}_2$ is the positive-semi-definite heat conductivity tensor as defined in the case of Fourier's law, the constant ξ_0 is the absolute entropy. Note that the dissipative component $\boldsymbol{q}_d$ of the heat flux satisfies the dissipation condition,

$$\boldsymbol{q}_d \cdot \nabla\Theta \leq 0. \tag{8}$$

Hence equation (4) together with the constitutive relations (5)–(7) and the thermal displacement–temperature relation (2) leads to the system of partial differential equations governing the distribution of temperature in space and time, $\Omega \times \mathbf{I}$, and is summarized as

$$\begin{aligned} \dot{\alpha} &= \Theta, \\ C\dot{\vartheta} &= -\operatorname{div} \boldsymbol{q} + \Theta^{-1} \boldsymbol{q}_e \cdot \nabla\Theta + r, \\ \boldsymbol{q} &= \boldsymbol{q}_e + \boldsymbol{q}_d, \text{ where } \boldsymbol{q}_e = -\Theta \boldsymbol{k}_1 \nabla\alpha, \ \boldsymbol{q}_d = -\boldsymbol{k}_2 \nabla\Theta. \end{aligned} \tag{9}$$

Furthermore, this system is subject to the initial condition for ϑ as

$$\vartheta(\boldsymbol{x}, 0) = \vartheta^0(\boldsymbol{x}), \qquad (\boldsymbol{x} \in \Omega). \tag{10}$$

Since we assume that the initial thermal displacement α^0 is uniform and the dependence of the temperature equation $(9)_2$ on α is only through its gradient $\nabla\alpha$, the temperature

[1]These equations are obtained when the hyperthermoelastic constitutive equations of neo-Hookean-type are extended to the generalized theory (see the article [34]) in the framework of the theory of Green and Naghdi [35–39], and specialized to the purely thermal case.

solution does not depend on the initial thermal displacement. As a consequence of this, in this work, for the sake of simplicity, we use a homogeneous initial condition for α, that is,

$$\alpha(\boldsymbol{x}, 0) = 0, \qquad (\boldsymbol{x} \in \Omega).$$

In addition, the system (9) is also supplemented with the boundary conditions

$$\begin{aligned} \vartheta &= \bar{\vartheta}, \qquad \text{on} \quad \Gamma_\vartheta \times \mathbf{I}, \\ \boldsymbol{q} \cdot \boldsymbol{n} &= q, \qquad \text{on} \quad \Gamma_q \times \mathbf{I}, \end{aligned}$$

where Γ_ϑ and Γ_q are mutually disjoint parts of the boundary Γ and $\boldsymbol{n}$ is a the outward unit normal to Γ.

2.2. Stability of the generalized model

Here we restrict our attention to the case that the system is solely driven by the initial condition such that the heat supply is homogeneous, $r = 0$, and the entire boundary is held at the reference temperature, that is, the relative temperature $\vartheta = 0$ on $\Gamma \times \mathbf{I}$. To define the state vector for system (9), we first redefine α by replacing $\alpha - \Theta_0 t$, $t \in \mathbf{I}$, for α such that equation $(9)_1$ becomes $\dot{\alpha} = \vartheta$. Thus we define the state vector as $\boldsymbol{\mathcal{X}} = (\alpha,\ \vartheta)$. Hence $\boldsymbol{\mathcal{X}}^* = \mathbf{0}$ becomes the equilibrium state for the system (9) at which the functional

$$V(\boldsymbol{\mathcal{X}}) = \int_\Omega \left[C(\vartheta - \Theta_0 \ln[\Theta/\Theta_0]) - \frac{1}{2\Theta} \boldsymbol{q}_e \cdot \nabla\alpha \right] \mathrm{d}\Omega, \tag{11}$$

vanishes. Note that V is positive-definite, that is, $V(\boldsymbol{\mathcal{X}}) > 0$ for all $\boldsymbol{\mathcal{X}}$ except at $\boldsymbol{\mathcal{X}}^* = \mathbf{0}$. To show the system is stable, it then suffices to prove that $\dot{V} \leq 0$ along the flow (or the solution). To this end, suppose $\boldsymbol{\mathcal{X}} = (\alpha,\ \vartheta)$ is the solution satisfying the conditions stipulated above; then from (11) and the constitutive equation (6) for $\boldsymbol{q}_e$ we obtain

$$\frac{\mathrm{d}}{\mathrm{d}t} V(\boldsymbol{\mathcal{X}}) = \int_\Omega \left[C\dot{\vartheta}\vartheta/\Theta - \Theta^{-1} \boldsymbol{q}_e \cdot \nabla\dot{\alpha} \right] \mathrm{d}\Omega, \tag{12}$$

Substitution of the thermal equation $(9)_2$ into (12) leads to

$$\frac{\mathrm{d}}{\mathrm{d}t}V(\boldsymbol{\mathcal{X}}) = \int_\Omega \left[(-\mathrm{div}\,\boldsymbol{q} + \Theta^{-1}\boldsymbol{q}_e\cdot\nabla\Theta)\vartheta/\Theta - \Theta^{-1}\boldsymbol{q}_e\cdot\nabla\Theta\right]\mathrm{d}\Omega, \tag{13}$$

$$= \int_\Omega \left[\boldsymbol{q}\cdot\nabla\Theta(1/\Theta - \vartheta/\Theta^2) + (\vartheta/\Theta^2)\boldsymbol{q}_e\cdot\nabla\Theta - \Theta^{-1}\boldsymbol{q}_e\cdot\nabla\Theta\right]\mathrm{d}\Omega \tag{14}$$

$$= \int_\Omega \left[(\boldsymbol{q}_e\cdot\nabla\Theta + \boldsymbol{q}_d\cdot\nabla\Theta)\Theta_0/\Theta^2 - (\Theta_0/\Theta^2)\boldsymbol{q}_e\cdot\nabla\Theta\right]\mathrm{d}\Omega$$

$$= \int_\Omega (\Theta_0/\Theta^2)\boldsymbol{q}_d\cdot\nabla\Theta\,\mathrm{d}\Omega$$

$$\leq 0 \tag{15}$$

Integration by parts along with the homogeneous boundary condition has been effected in passing from (13) to (14), and the inequality (15) follows from the dissipation condition, equation (8).

3. Space-time Galerkin methods

Denoting the space-time domain $\Omega \times \mathbf{I}$ by $\mathbb{\Omega}$, we partition the space-time domain into slabs of the form $\mathbb{\Omega}_n = \Omega \times I_n$ such that

$$\mathbb{\Omega} = \bigcup_{n=1}^{\tilde{N}} \mathbb{\Omega}_n, \quad \text{and} \quad I_n = [t_{n-1},\ t_n],$$

where $\tilde{N}$ is the the number of slabs in the partition. Furthermore, the nth space-time slab is $\mathbb{\Omega}_n$ triangulated into K_n space-time finite elements (which could be entirely unstructured), where the eth space-time element in the triangulation of $\mathbb{\Omega}_n$ is denoted by $\mathbb{\Omega}_n^e$. The following notations are introduced, let ϕ and φ be scalar valued functions defined on the space-time domain $\mathbb{\Omega}$, then

$\mathbb{\Gamma}_{\varphi}^{n} = \Gamma \times I_n$ – the nth slab dirichlet boundary

$\mathbb{\Gamma}_{q}^{n} = \Gamma \times I_n$ – the nth slab Neumann boundary

$\phi(t^{\pm}) = \lim\limits_{\substack{h \to 0 \\ h>0}} \phi(\cdot,\, t \pm h)$ – value earlier/later than t

$[\![\phi(t)]\!] = \phi(t^{+}) - \phi(t^{-})$ – temporal jump at time t

$\big(\phi,\, \varphi\big)_{\mathbb{\Omega}_n} = \int_{\mathbb{\Omega}_n} \phi\, \varphi \, \mathrm{d}\mathbb{\Omega}$ – space-time integral inner-product

$\langle \phi(\cdot,\, t),\, \varphi(\cdot,\, t) \rangle = \int_{\Omega} \phi(\cdot,\, t)\, \varphi(\cdot,\, t) \, \mathrm{d}\Omega$ – spatial integral inner-product

$(\phi,\, \varphi)_{\mathbb{\Gamma}_q^n} = \int_{\mathbb{\Gamma}_q^n} \phi\, \varphi \, \mathrm{d}\mathbb{\Gamma}$ – space-time surface integral inner-product

In the remaining part of this section, we present two methods belonging to the family of space-time Galerkin finite element methods. The first is the time-discontinuous Galerkin (TDG FE); the second is continuous Galerkin (cG FE).

3.1. Time-discontnuous Galerkin method (TDG FE)

Here, the primary fields (in this case α and ϑ) are allowed to be discontinuous along any space-time interfaces between slabs. This is intended to give better stability properties, particularly when the solution involves propagation of steep gradients or even discontinuities. This is an extension of the time-discontinuous formulation that we employed in [51] for the generalized linear thermoelasticity to the nonlinear case.

Suppose the problem is already solved on the slab $\mathbb{\Omega}_{n-1}$ or, in particular, the solution

$\boldsymbol{\mathcal{X}}^h(t_{n-1}^-)$ from the left of t_{n-1} is known. To proceed with the formulation of the TDG FE, we first define the trial $\mathcal{V}_{DG}^h$ and weighting $\mathcal{W}_{DG}^h$ spaces as follows:

$$\mathcal{V}_{DG}^h \coloneqq \{\boldsymbol{\mathcal{X}}^h = (\alpha^h,\, \vartheta^h) \in [C^0(\mathfrak{I}_n)]^2 :\ \alpha^h|_{\mathfrak{I}_n^e} \in \mathcal{P}^k(\mathfrak{I}_n^e),\, \vartheta^h|_{\mathfrak{I}_n^e} \in \mathcal{P}^l(\mathfrak{I}_n^e), \text{and } \vartheta^h = \bar{\vartheta} \text{ on } \mathbb{\Gamma}_\vartheta^n\}, \tag{16}$$

$$\mathcal{W}_{DG}^h \coloneqq \{\widehat{\boldsymbol{\mathcal{X}}}^h = (\widehat{\alpha}^h,\, \widehat{\vartheta}^h) \in [C^0(\mathfrak{I}_n)]^2 :\ \widehat{\alpha}^h|_{\mathfrak{I}_n^e} \in \mathcal{P}^k(\mathfrak{I}_n^e),\, \widehat{\vartheta}^h|_{\mathfrak{I}_n^e} \in \mathcal{P}^l(\mathfrak{I}_n^e), \text{and } \widehat{\vartheta}^h = 0 \text{ on } \mathbb{\Gamma}_\vartheta^n\}, \tag{17}$$

where $\mathcal{P}^k(\mathfrak{I}_n)$ denotes the set of all polynomials on $\mathfrak{I}_n$ of degree at most k. Generally, there is no restriction on the order of the polynomial spaces for temperature, l, and thermal displacement, k, interpolation spaces. Note also that there are no constraints placed on the trial and weighting spaces at the beginning of the space-time slab ($\Omega \times \{t_{n-1}\}$), because the values $\boldsymbol{\mathcal{X}}^h(t_{n-1}^+)$ are unknown with respect to the current slab $\mathfrak{I}_n$. This represents the largest possible number of candidates to obtain an approximation that would improve that of a space-time Bubnov-Galerkin–type approach.

Now, we formally define the TDG FE scheme as follows: find $\boldsymbol{\mathcal{X}}^h \in \mathcal{V}_{DG}^h$ such that for each $\widehat{\boldsymbol{\mathcal{X}}}^h \in \mathcal{W}_{DG}^h$,

$$L_{DG}(\boldsymbol{\mathcal{X}}^h,\, \widehat{\boldsymbol{\mathcal{X}}}^h) = \ell_{DG}(\widehat{\boldsymbol{\mathcal{X}}}^h), \tag{18}$$

where the nonlinear functional L_{DG} and the right-hand-side ℓ_{DG} are given by

$$\begin{aligned} L_{DG}(\boldsymbol{\mathcal{X}}^h,\, \widehat{\boldsymbol{\mathcal{X}}}^h) = {} & \big(\dot{\alpha}^h - \Theta^h,\, \widehat{\alpha}^h\big)_{\mathfrak{I}_n} + \langle \alpha^h(t_{n-1}^+),\, \widehat{\alpha}^h(t_{n-1}^+)\rangle + \big(C\dot{\vartheta}^h,\, \widehat{\vartheta}^h\big)_{\mathfrak{I}_n} - \big(\boldsymbol{q}^h,\, \nabla\widehat{\vartheta}^h\big)_{\mathfrak{I}_n} - \\ & \big([1/\Theta^h]\boldsymbol{q}_e^h \cdot \nabla\Theta^h,\, \widehat{\vartheta}^h\big)_{\mathfrak{I}_n} + \langle C\vartheta^h(t_{n-1}^+),\, \widehat{\vartheta}^h(t_{n-1}^+)\rangle, \end{aligned}$$

$$\begin{aligned} \ell_{DG}(\widehat{\boldsymbol{\mathcal{X}}}) = {} & \langle \alpha^h(t_{n-1}^-),\, \widehat{\alpha}^h(t_{n-1}^+)\rangle + \langle C\vartheta^h(t_{n-1}^-),\, \widehat{\vartheta}^h(t_{n-1}^+)\rangle + \\ & \big(r,\, \widehat{\vartheta}^h\big)_{\mathfrak{I}_n} - \big(q^h,\, \widehat{\vartheta}^h\big)_{\mathbb{\Gamma}_q^n}. \end{aligned}$$

Note that Θ^h, $\boldsymbol{q}^h$, $\boldsymbol{q}_e^h$ denote approximations of the absolute temperature, heat flux, and energetic part of the heat flux, respectively, that are obtained from the finite element interpolations α^h and ϑ^h.

The *consistency* of the TDG FE scheme can be shown by converting the equation (18) into an Euler-Lagrange form by using integration by parts: that is,

$$
\begin{aligned}
0 \;&=\; L_{DG}(\boldsymbol{\mathcal{X}}^h,\, \widehat{\boldsymbol{\mathcal{X}}}^h) - \ell_{DG}(\widehat{\boldsymbol{\mathcal{X}}}), && \text{(Residual)} \\
&=\; \big(\dot{\alpha}^h - \Theta^h,\, \widehat{\alpha}^h\big)_{\Omega_n} \\
&\quad + \big(C\dot{\vartheta}^h + \operatorname{div} \boldsymbol{q}^h - [1/\Theta^h]\boldsymbol{q}_e^h \cdot \nabla\Theta^h - r,\, \widehat{\vartheta}^h\big)_{\Omega_n} && \left.\begin{array}{l}\\ \\ \end{array}\right\} \text{(Equation of motion)} \\
&\quad + \langle [\![\alpha^h(t_{n-1})]\!],\, \widehat{\alpha}^h(t_{n-1}^+)\rangle && (\alpha^h\text{–continuity}) \\
&\quad + \langle C[\![\vartheta^h(t_{n-1})]\!],\, \widehat{\vartheta}^h(t_{n-1}^+)\rangle. && (\vartheta^h\text{–continuity})
\end{aligned}
$$

Here the jump terms are used to weakly enforce continuity along the interfaces of space-time slabs, and vanish if the solutions are continuous. Hence, we can observe that a sufficiently smooth solution $\boldsymbol{\mathcal{X}} = (\alpha, \vartheta)$ of the strong form (9) satisfies the above Euler-Lagrange form.

The TDG FE scheme renders a nonlinear time-stepping algorithm. A crucial property in any time-stepping algorithms is *stability*. It refers to the question as to how errors grow as the algorithm marches forward in time. For nonlinear algorithms, one way of proving stability is the so-called *energy method*, which involves showing existence of a *Lyapunov function*, a positive-definite functional that is non-increasing along the numerical solution. In our case, this means that the numerical solution should also replicate the stability property (13)-(15) of the strong form of the problem (9) in the discrete sense. This will be discussed in the following section.

3.2. Stability of the TDG FE scheme

As in the case of the stability analysis (9) of the strong form, here we also assume homogeneous Dirchlet boundary condition over the entire boundary, and without heat source, whereby the system is only driven by the initial condition (10). One of the remarkable features of the TDG FE formulation is that the energy functional (11) for the strong form is also a Lyapunov function for the discrete TDG FE algorithm (18). To show this, since V is positive-definite, what remains to prove is that it is non-increasing along the discrete solution of (18), that is,

$$
V(\boldsymbol{\mathcal{X}}^h(t_n^-)) \leq V(\boldsymbol{\mathcal{X}}^h(t_{n-1}^-)) \;\; \text{or} \;\; V(\boldsymbol{\mathcal{X}}^h(t_n^+)) \leq V(\boldsymbol{\mathcal{X}}^h(t_{n-1}^+)), \tag{19}
$$

where $\boldsymbol{\mathcal{X}}^h(t_{n-1}^{\pm})$ and $\boldsymbol{\mathcal{X}}^h(t_n^{\pm})$ are solutions of the TDG FE scheme (18). The statements (19) should hold for all $n = 1, \ldots, N$. Since both estimates employ similar arguments, without loss of generality, we will only prove the validity of the first estimate of (19). Let $\boldsymbol{\mathcal{X}}^h = (\alpha^h, \vartheta^h)$ be the solution of TDG FE scheme (18) in the current slab $\mathbb{\Omega}_n$. It should be noted that because of the assumption on the boundary condition, the trial (16) and weighting (17) spaces are the same, that is, $\mathcal{V}_{DG}^h = \mathcal{W}_{DG}^h$. Now, if we choose the weighting function $\widehat{\boldsymbol{\mathcal{X}}}^h$ to be equal to $\boldsymbol{\Pi}^h(\mathrm{div}\,[1/\Theta^h \boldsymbol{q}_e^h],\, \vartheta^h/\Theta^h)$, from the residual of the TDG FE formulation (18) we obtain

$$
\begin{aligned}
&\big(\dot{\alpha}^h - \Theta^h,\, \boldsymbol{\pi}^h \mathrm{div}\,[(1/\Theta^h)\boldsymbol{q}_e]\big)_{\mathbb{\Omega}_n} + \big(C\dot{\vartheta}^h,\, \boldsymbol{\pi}^h[\vartheta^h/\Theta^h]\big)_{\mathbb{\Omega}_n} \\
&- \big(\boldsymbol{q}_e + \boldsymbol{q}_d,\, \nabla\boldsymbol{\pi}^h[\vartheta^h/\Theta^h]\big)_{\mathbb{\Omega}_n} - \big([1/\Theta^h]\boldsymbol{q}_e \cdot \nabla\Theta^h,\, \vartheta^h/\Theta^h\big)_{\mathbb{\Omega}_n} \\
&+ \langle [\![\alpha^h(t_{n-1})]\!],\, \boldsymbol{\pi}^h \mathrm{div}\,[(1/\Theta^h(t_{n-1}^+))\boldsymbol{q}_e(t_{n-1}^+)]\rangle \\
&+ \langle C[\![\vartheta^h(t_{n-1})]\!],\, \vartheta^h(t_{n-1}^+)/\Theta^h(t_{n-1}^+)\rangle = 0,
\end{aligned}
\tag{20}
$$

where $\boldsymbol{\Pi}^h = (\boldsymbol{\pi}^h,\, \boldsymbol{\pi}^h)$ is the L^2-projection operator from $[L^2(\mathbb{\Omega}_n)]^2$ onto the finite dimensional space $\mathcal{W}^h$. Note also that $1/\Theta^h \boldsymbol{q}_e^h = -\boldsymbol{k}_1 \nabla\alpha^h$. By definition of the L^2-projection operator and making use of integration by parts along with the homogeneous boundary condition, equation (20) becomes

$$
\begin{aligned}
&- \big(\nabla\dot{\alpha}^h - \nabla\Theta^h,\, [1/\Theta^h]\boldsymbol{q}_e\big)_{\mathbb{\Omega}_n} + \big(C\dot{\vartheta}^h,\, \vartheta^h/\Theta^h\big)_{\mathbb{\Omega}_n} \\
&- \big(\boldsymbol{q}_e + \boldsymbol{q}_d,\, (1/\Theta^h - \vartheta^h/[\Theta^h]^2)\nabla\Theta^h\big)_{\mathbb{\Omega}_n} - \big((\vartheta^h/[\Theta^h]^2)\boldsymbol{q}_e,\, \nabla\Theta^h\big)_{\mathbb{\Omega}_n} \\
&+ \langle [\![\nabla\alpha^h(t_{n-1})]\!],\, \boldsymbol{k}_1\nabla\alpha^h(t_{n-1}^+)\rangle \\
&+ \langle C[\![\vartheta^h(t_{n-1})]\!],\, \vartheta^h(t_{n-1}^+)/\Theta^h(t_{n-1}^+)\rangle = 0.
\end{aligned}
$$

By eliminating similar terms with opposite sign and after rearranging the remaining terms, we obtain that

$$
\begin{aligned}
&\big(C\dot{\vartheta}^h,\, \vartheta^h/\Theta^h\big)_{\mathbb{\Omega}_n} - \big(\nabla\dot{\alpha}^h,\, [1/\Theta^h]\boldsymbol{q}_e\big)_{\mathbb{\Omega}_n} - \big(\boldsymbol{q}_d,\, (\Theta_0/[\Theta^h]^2)\nabla\Theta^h\big)_{\mathbb{\Omega}_n} \\
&+ \langle [\![\nabla\alpha^h(t_{n-1})]\!],\, \boldsymbol{k}_1\nabla\alpha^h(t_{n-1}^+)\rangle + \langle C[\![\vartheta^h(t_{n-1})]\!],\, \vartheta^h(t_{n-1}^+)/\Theta^h(t_{n-1}^+)\rangle = 0.
\end{aligned}
\tag{21}
$$

In equation (21) the first two terms are the integral of the time derivative of V over the time interval I_n. We write V as

$$V(\boldsymbol{\mathcal{X}}) = \int_\Omega [U_1(\vartheta) + U_2(\nabla\alpha)]\mathrm{d}\Omega, \tag{22}$$

$$\text{with} \quad U_1(\vartheta) = C(\vartheta - \Theta_0 \ln[\Theta/\Theta_0]),$$

$$U_2(\nabla\alpha) = -\frac{1}{2\Theta}\boldsymbol{q}_e \cdot \nabla\alpha = \frac{1}{2}\boldsymbol{k}_1 \nabla\alpha \cdot \nabla\alpha,$$

where it can easily be shown that both U_1 and U_2 are convex in their respective arguments, and their derivatives are

$$U_1'(\vartheta) = C\vartheta/\Theta, \quad \text{and} \quad U_2'(\nabla\alpha) = \boldsymbol{k}_1\nabla\alpha.$$

Hence equation (21) becomes

$$\int_{t_{n-1}}^{t_n} \frac{\mathrm{d}}{\mathrm{d}t} V(\boldsymbol{\mathcal{X}}^h)\,\mathrm{d}t - \left(\boldsymbol{q}_d,\, (\Theta_0/[\Theta^h]^2)\nabla\Theta^h\right)_{\Omega_n}$$
$$+ \int_\Omega U_1'(\vartheta^h(t_{n-1}^+))[\![\vartheta^h(t_{n-1})]\!]\,\mathrm{d}\Omega + \int_\Omega U_2'(\nabla\alpha^h(t_{n-1}^+))[\![\nabla\alpha^h(t_{n-1})]\!]\,\mathrm{d}\Omega = 0. \tag{23}$$

By convexity of U_1 and U_2 and evaluating the temporal integral, from (23) one obtains

$$V(\boldsymbol{\mathcal{X}}^h(t_n^-)) - V(\boldsymbol{\mathcal{X}}^h(t_{n-1}^+)) - \left(\boldsymbol{q}_d,\, (\Theta_0/[\Theta^h]^2)\nabla\Theta^h\right)_{\Omega_n}$$
$$+ \int_\Omega [U_1(\vartheta^h(t_{n-1}^+)) - U_1(\vartheta^h(t_{n-1}^-))]\,\mathrm{d}\Omega$$
$$+ \int_\Omega [U_2(\nabla\alpha^h(t_{n-1}^+)) - U_2(\nabla\alpha^h(t_{n-1}^-))]\,\mathrm{d}\Omega \le 0. \tag{24}$$

From (22) and (24), it follows that

$$V(\boldsymbol{\mathcal{X}}^h(t_n^-)) - V(\boldsymbol{\mathcal{X}}^h(t_{n-1}^+)) - \left(\boldsymbol{q}_d,\, (\Theta_0/[\Theta^h]^2)\nabla\Theta^h\right)_{\Omega_n} +$$
$$V(\boldsymbol{\mathcal{X}}^h(t_{n-1}^+)) - V(\boldsymbol{\mathcal{X}}^h(t_{n-1}^-)) \le 0.$$

Thus,

$$V(\boldsymbol{\mathcal{X}}^h(t_n^-)) - \left(\boldsymbol{q}_d,\, (\Theta_0/[\Theta^h]^2)\nabla\Theta^h\right)_{\Omega_n} \le V(\boldsymbol{\mathcal{X}}^h(t_{n-1}^-)). \tag{25}$$

Therefore, by the dissipation inequality (8), it follows that equation (25) leads to the required energy estimate; that is,

$$V(\boldsymbol{\mathcal{X}}^h(t_n^-)) \le V(\boldsymbol{\mathcal{X}}^h(t_{n-1}^-)).$$

3.3. Continuous Galerkin method (cG FE)

Here the primary fields are assumed to be continuous over the entire space-time domain $\mathbb{\Omega}$. But still the space-time domain is partitioned into slabs as in the case of TDG FE method, and the algorithm proceeds slab-by-slab in a time-stepping manner. Even though the lack of jump terms reduces the ability of the cG FE method to resolve high gradients and discontinuities as much as the TDG FE method the algorithm, as will be shown later, is still unconditionally stable.

Suppose that the solution $\boldsymbol{\mathcal{X}}^h(t_{n-1})$ from the previous slab $\mathbb{\Omega}_{n-1}$ at t_{n-1} is known. We would like to obtain a scheme for obtaining an approximate solution in the current slab $\mathbb{\Omega}_n$ with no jump discontinuity at t_{n-1}. We first define the weighting $\mathcal{W}^h_{cG}$ and the trial $\mathcal{V}^h_{cG}$ solution spaces as follows by

$$\begin{aligned}\mathcal{V}^h_{cG} \coloneqq \{\boldsymbol{\mathcal{X}}^h =&(\alpha^h,\, \vartheta^h) \in [C^0(\mathbb{\Omega}_n)]^2 :\ \alpha^h|_{\mathbb{\Omega}^e_n} \in \mathcal{P}^k(\mathbb{\Omega}^e_n),\, \vartheta^h|_{\mathbb{\Omega}^e_n} \in \mathcal{P}^l(\mathbb{\Omega}^e_n),\\ &\vartheta^h = \bar{\vartheta} \text{ on } \mathbb{\Gamma}^n_\vartheta,\ \text{and } \boldsymbol{\mathcal{X}}^h(t^+_{n-1}) = \boldsymbol{\mathcal{X}}^h(t^-_{n-1}) \text{ in } \Omega\}, \qquad (26)\\ \mathcal{W}^h_{cG} \coloneqq \{\widehat{\boldsymbol{\mathcal{X}}}^h =&(\widehat{\alpha}^h,\, \widehat{\vartheta}^h) \in [C^0(\mathbb{\Omega}_n)]^2 :\ \widehat{\alpha}^h|_{\mathbb{\Omega}^e_n} \in \mathcal{P}^k(\mathbb{\Omega}^e_n),\, \widehat{\vartheta}^h|_{\mathbb{\Omega}^e_n} \in \mathcal{P}^l(\mathbb{\Omega}^e_n),\\ &\widehat{\vartheta}^h = 0 \text{ on } \mathbb{\Gamma}^n_\vartheta \text{ and } \boldsymbol{\mathcal{X}}^h(t^+_{n-1}) = \mathbf{0} \text{ in } \Omega\}, \qquad (27)\end{aligned}$$

Then the continuous Galerkin method (cG FE) is formulated as: find $\boldsymbol{\mathcal{X}}^h \in \mathcal{V}^h_{cG}$ such that for all $\bar{\boldsymbol{\mathcal{X}}}^h \in \mathcal{W}^h_{cG}$

$$L_{cG}(\boldsymbol{\mathcal{X}}^h,\, \bar{\boldsymbol{\mathcal{X}}}^h) = \ell_{cG}(\boldsymbol{\mathcal{X}}^h), \qquad (28)$$

where

$$L_{cG}(\boldsymbol{\mathcal{X}}^h,\, \bar{\boldsymbol{\mathcal{X}}}^h) = \big(\dot{\alpha}^h - \Theta^h,\, \widehat{\alpha}^h\big)_{\mathbb{\Omega}_n} + \big(C\dot{\vartheta}^h,\, \widehat{\vartheta}^h\big)_{\mathbb{\Omega}_n} - \big(\boldsymbol{q}^h,\, \nabla\widehat{\vartheta}^h\big)_{\mathbb{\Omega}_n} - \big([1/\Theta^h]\boldsymbol{q}^h_e \cdot \nabla\Theta^h,\, \widehat{\vartheta}^h\big)_{\mathbb{\Omega}_n}$$

$$\ell_{cG}(\widehat{\boldsymbol{\mathcal{X}}}) = \big(r,\, \widehat{\vartheta}^h\big)_{\mathbb{\Omega}_n} - \big(q^h,\, \widehat{\vartheta}^h\big)_{\mathbb{\Gamma}^n_q}.$$

We note that due to the constraints placed on the finite element spaces (26) and (27) at the lower interface of the current space-time slab $\mathbb{\Omega}_n$, that is at t_{n-1}, the trial space in the case of cG FE case is smaller than that of the TDG FE case. Thus, there are more candidate solutions to choose from for TDG FE than cG FE scheme. As a consequence of this, for

the same order of polynomial interpolation, one would expect the TDG FE scheme to be more accurate than the cG FE method. On the other hand, it is less expensive to solve the cG FE solution as it is not necessary to recompute the solution at the lower interface of the current slab.

Remarks

1. Inter-slab interface continuity is enforced strongly through the definition of the finite element interpolation functions unlike in the TDG FE case where continuity is enforced weakly using the spatial L^2-inner product.

2. Consistency of the cG FE formulation (28) can be easily shown by rewriting it in the Euler-Lagrange form, which reveals that the discrete formulation is indeed a weak form of (9) in space-time.

3. The nonlinear stability proof of the scheme (28) is quite similar to that of the TDG FE case, except that, in this case, there are no jumps and the equation analogous to (21) is

$$\left(C\dot{\vartheta}^h,\, \vartheta^h/\Theta^h\right)_{\Omega_n} - \left(\nabla\dot{\alpha}^h,\, [1/\Theta^h]\boldsymbol{q}_e\right)_{\Omega_n} - \left(\boldsymbol{q}_d,\, (\Theta_0/[\Theta^h]^2)\nabla\Theta^h\right)_{\Omega_n} = 0,$$

   which can also be written as

$$\int_{t_{n-1}}^{t_n} \frac{\mathrm{d}}{\mathrm{d}t} V(\boldsymbol{\mathcal{X}}^h)\,\mathrm{d}t - \left(\boldsymbol{q}_d,\, (\Theta_0/[\Theta^h]^2)\nabla\Theta^h\right)_{\Omega_n} = 0.$$

   Integrating the first term over the time interval I_n and by using the fact that inter-slab interface continuities are enforced strongly, we obtain

$$V(\boldsymbol{\mathcal{X}}^h(t_n^-)) - V(\boldsymbol{\mathcal{X}}^h(t_{n-1}^-)) - \left(\boldsymbol{q}_d,\, (\Theta_0/[\Theta^h]^2)\nabla\Theta^h\right)_{\Omega_n} = 0.$$

   Again by dissipation inequality (8), the required energy estimate $(19)_1$ is obtained.

4. The TDG FE scheme is characterized by the presence of the jump terms which offer superior stability properties, while in the cG FE case there are no additional stability mechanisms except through the dissipation condition (8).

4. Numerical results

In this section, we consider isotropic materials so that the conductivity tensors take the form $\boldsymbol{k}_1 = k_1\mathbf{1}, \boldsymbol{k}_2 = k_2\mathbf{1}$, where $k_1 > 0$, $k_2 \geq 0$, and $\mathbf{1}$ is the identity second-order tensor. All results in this section correspond to a non-dimensional form of the governing equations (9) such that the thermal displacement, temperature and heat flux are redefined in non-dimensional form as

$$\tilde{\alpha} = \frac{\alpha}{\tau\Theta_0}, \quad \tilde{\vartheta} = \frac{\vartheta}{\Theta_0}, \quad \tilde{\boldsymbol{q}} = \frac{\tau_0\Theta_0}{l_0 C}\boldsymbol{q}, \tag{29}$$

where τ_0 and l_0 are the characteristic time and length scales involved, for which the space and time coordinates are redefined as

$$\tilde{\boldsymbol{x}} = \frac{1}{l_0}\boldsymbol{x}, \text{ and } \tilde{t} = \frac{t}{\tau_0}. \tag{30}$$

For clarity, we drop the tildes from the non-dimensional quantities in the remainder of this section.

4.1. Convergence study

To investigate the convergence of the proposed schemes, we consider the one-spatial dimension, linearized and non-dimensional form of (9), that is

$$\left.\begin{aligned} \dot{\alpha} &= \vartheta \\ \dot{\vartheta} &= \partial_x[k_1\partial_x\alpha + k_2\partial_x\vartheta] + r \end{aligned}\right\} \quad \text{in} \quad [0,\,1]\times[0,\,1], \tag{31}$$

where k_1, k_2, and r are non-dimensional constants according to the scaling in (29) and (30), and ∂_x denotes the partial derivative with respect to x. Moreover, we choose a source term and appropriate initial and boundary conditions so that the exact solutions for (31) are

$$\begin{aligned} \alpha &= \frac{1}{4}\sin(2\pi x)\sin(2\pi t) \\ \vartheta &= \frac{\pi}{2}\sin(2\pi x)\cos(2\pi t). \end{aligned}$$

The corresponding source term r can be easily computed by substituting these solutions into the the linearized system (31).

The energy norm corresponding to the linearized system (31) is thus given by

$$\|\boldsymbol{\mathcal{X}}\|^2 = \int_0^1 \left(k_1[\partial_x \alpha]^2 + \vartheta^2\right) \mathrm{d}x, \tag{32}$$

where $\boldsymbol{\mathcal{X}} = (\alpha,\, \vartheta)$. This norm is used to compute the error of approximations $\boldsymbol{\mathcal{X}}^h = (\alpha^h,\, \vartheta^h)$ at the terminal time $t = 1$.

Though the TDG and cG FE formulation allows for the grid in each space-time slab to be completely unstructured, for comparison purpose, the results presented in Figures 1 – 3 correspond to computations in which the space-time mesh is composed of slabs with $N = 1$, each of which is refined uniformly into elements of unit aspect ratio. In each case, the left side corresponds to computations with Q1 space-time elements, while those on the right side corresponds to biquadratic Q2 space-time elements.

It has been noted that the weak enforcement of continuity through the jump terms in the TDG FE scheme are important for stability as well as accuracy. The TDG scheme proposed by Hulbert and Hughes [55] and Hughes and Hulbert [56] for second-order hyperbolic problems is stable only if the space-time mesh consists of slabs of single layer, $N = 1$, [53], whereas, the similar formulation by Khalmonova and Costanzo [53] for coupled linear thermoelasticity exhibits dependence of accuracy on N. In contrast, the result for the TDG FE scheme as shown in Figure 4 demonstrates that, in addition to the unconditional stability behavior as proved in Sec. 3.2, irrespective of the mesh structure, its accuracy is independent of N.

Figure 1 presents the convergence results for the Type I equation (i.e. $k_1 = 0$, or the classical transient heat conduction problem) as computed by all the two schemes proposed, with single layered slabs, $N = 1$. Note that in this case, as $k_1 = 0$, the energy norm coincides with the L^2 norm with respect to the temperature only. As a result, the result shows slightly better rate of convergence, compared to the same type of approximations for Type II and III. The results corresponding to Type II and III in Figure 2 & 3 suggest that the order of TDG FE scheme is at least $\mathcal{O}(h^q)$, where h is the diameter of the largest element and q is the highest monomial degree appearing in the piece-wise polynomial finite element space.

Figure 4 shows convergence results of both TDG FE (left) and cG FE (right) schemes for

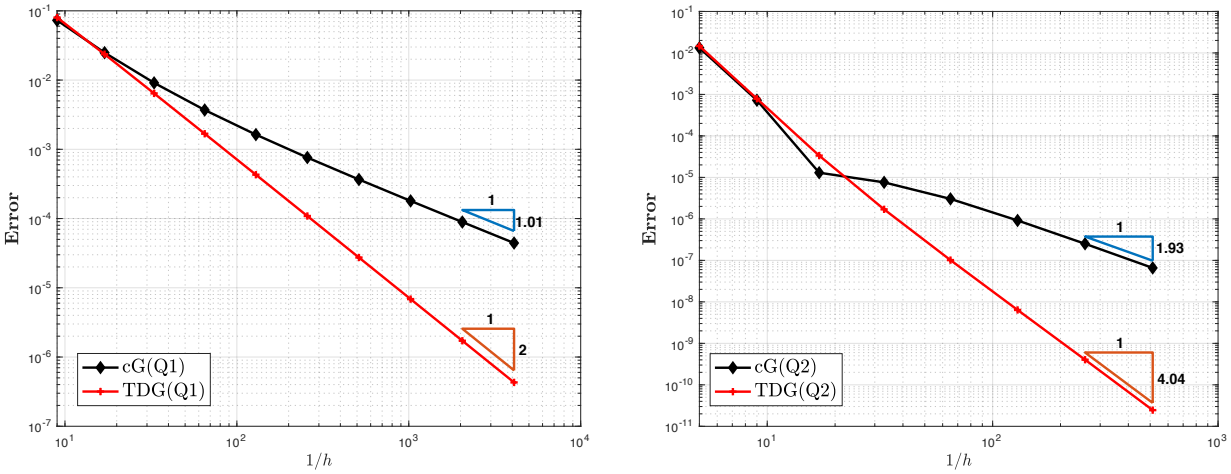

Figure 1: Convergence results for the Type I problem in 1D in which $k_1 = 0$, $k_2 = 1$. The space-time domains were uniformly refined into rectangular elements with aspect ratio one, or $h = \Delta x = \Delta t$, and each slab consists of single layer ($N = 1$). Space-time elements of type Q1 (left) and Q2 (right) were used. The label '**Error**' represents the energy norm (32) of the error.

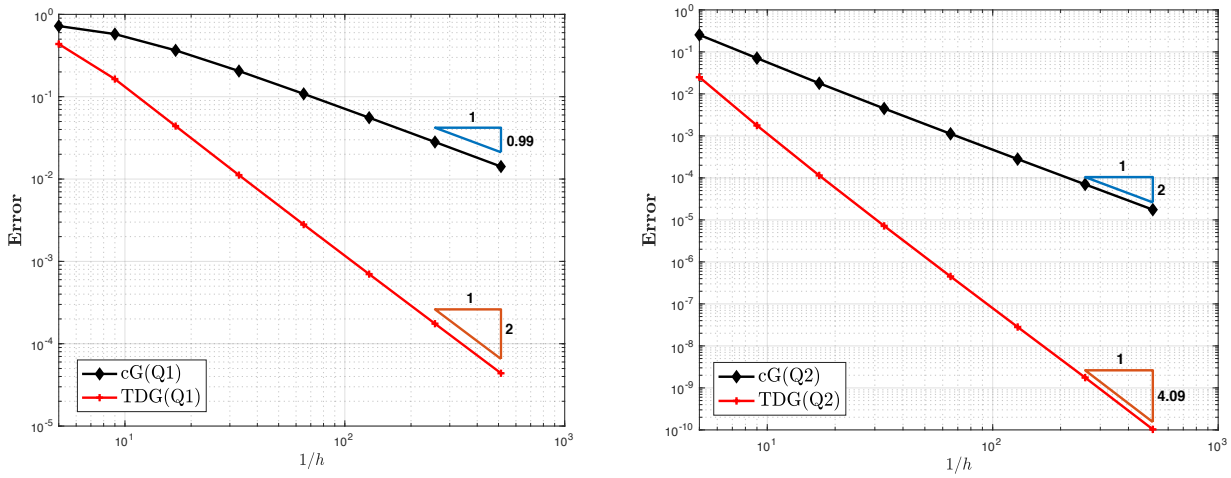

Figure 2: Convergence results for the Type II problem (the non-classical theory of Green and Naghdi) characterized by the absence of dissipation in 1D in which $k_1 = 1$, $k_2 = 0$. The space-time domains were uniformly refined into rectangular elements of bilinear-type or Q1 (left) and biquadratic-type Q2 (right) with aspect ratio one, or $h = \Delta x = \Delta t$. The label '**Error**' represents the energy norm (32) of the error.

Type III problem for which each curve corresponds to uniformly refined slabs of thickness of $2, 4, 8, 16, 32$ elements with both Q1 and Q2 approximations. The fact that the curves (on the left) corresponding to Q1 and Q2 approximations are observed to overlap one another suggests that, in TDG FE approximations, neither the accuracy nor the convergence rate depend on N. The implication of this remarkable property of TDG FE scheme is that it is suitable for local space-time mesh adaptation without losing accuracy when the mesh uses variable temporal thickness, N, on various regions of a space-time slab. Hence, one can get an efficient TDG FE scheme by refining only regions of the space-time slab that need to be refined, leaving the rest with only one element layer, $N = 1$.

On the other hand, for each N, the result in Figure 4 (right) corresponding to cG FE (Q2) shows that the error deteriorates towards the beginning the refinement levels as the computation involves stepping over a multiple number of slabs, and the convergences tend second-order asymptotically in both the Q1 and Q2. This dependance on the number of slabs suggests two things: 1) stability of the cG FE scheme becomes less as the order of the space-time finite element is higher, and 2) the accuracy of cG FE is restricted to only to second-order even with higher-order (Q2) finite elements.

4.2. Two-dimensional laser-pulsing in a rigid body

Non-Fourier type thermal transport occurs rarely and previously limited to a handful of materials such as super-fluids and pure crystals at low temperatures. In recent experimental study [62] second-sound phenomenon has been directly observed in graphite at temperatures above 100 kelvins. In another recent experimental work [63] a non-Fourier effect that involve thermal energy propagation without energy dissipation has been achieved at room temperature. This work made use of a device referred to as "thermal inductor" that can drive temperature differences between two bodies to change signs by imposing inertia on the heat flowing between them.

Here we consider the propagation of thermal waves induced by a pulsing laser heat source in a rigid body. This set of problems has been investigated by several other researchers, for instance in [1, 21] it was analyzed using the linear hyperbolic heat conduction model of

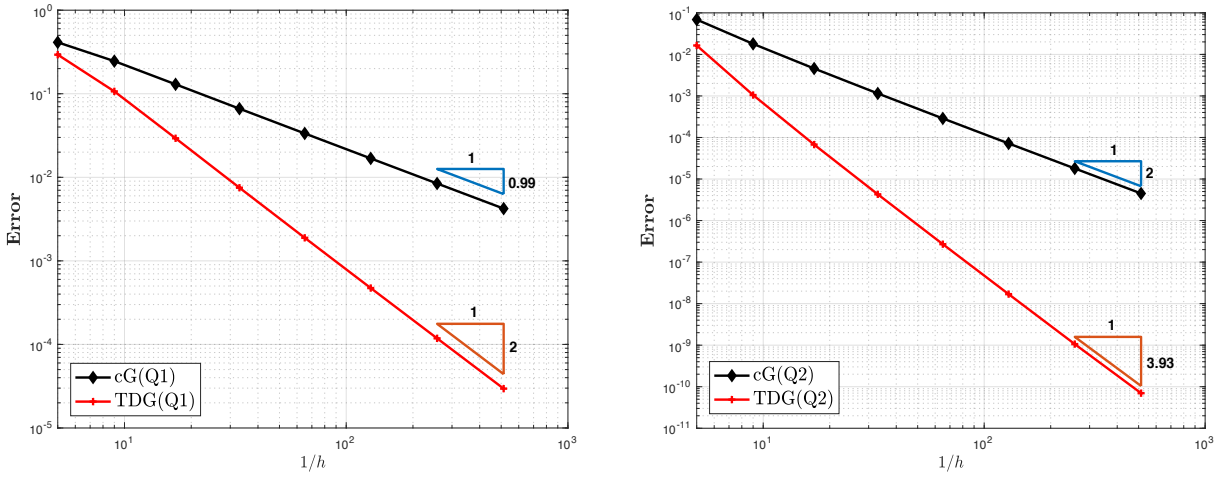

Figure 3: Convergence results for the Type III problem (the generalized thermal conduction equation) in 1D in which $k_1 = 0$, $k_2 = 1$. The space-time domains were uniformly refined into rectangular elements of bilinear-type Q1 (right) and biquadratic-type Q2 (left) with unit aspect ratio, or $h = \Delta x = \Delta t$. The label '**Error**' represents the energy norm (32) of the error at the terminal time $t = 1$.

Cattaneo-Vernotte-Maxwell.

All the results presented in this section correspond to the non-dimensional form of the equations in (9) according to the scaling (29) and (30).

The nonlinearity of the governing partial differential equations lies in the constitutive relation for the energetic heat flux $\boldsymbol{q}_e$ equation (6). This represents the typical nonlinear behaviour that is present in the well-known *inviscid Burger's equation*, in which the characteristic speed is proportional to the value of the temperature ϑ. This is equivalent to stating that a point at a higher temperature the rate is faster than those at lower temperatures. This characteristic of the propagation of thermal waves is manifested by the sharpness of the wave front as it travels in a medium. Here we emphasize that the nonlinearity present in the current model is not a mathematical artifact, rather it is naturally present as a consequence of the laws of thermodynamics.

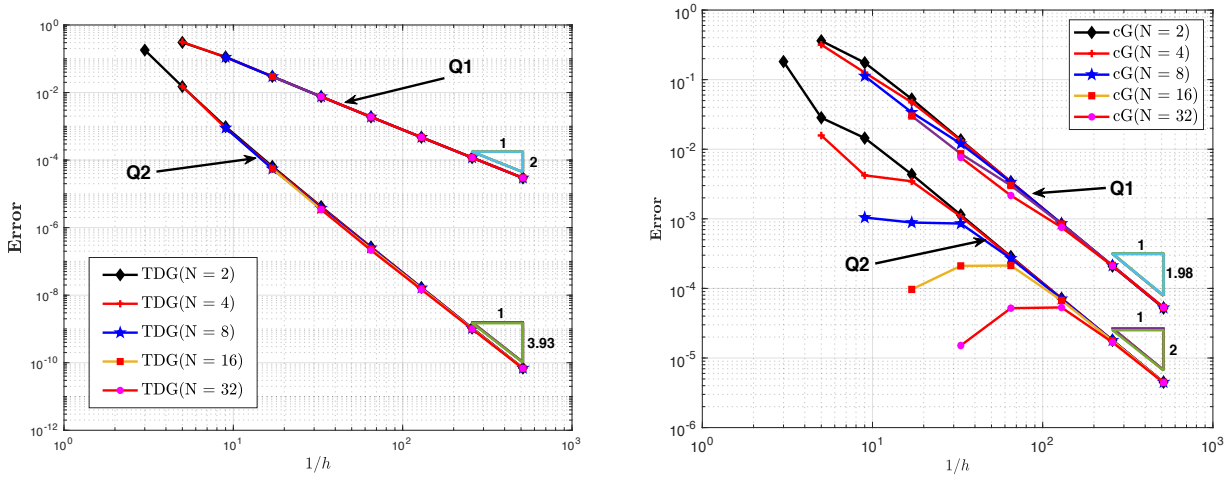

Figure 4: Convergence results for the Type III problem (the generalized equation) in 1D in which $k_1 = 1$, $k_2 = 0.2$. The band of curves labelled 'Q1' (resp. 'Q2') correspond to calculations with space-time elements of type Q1 (resp. Q2), and element layers per slabs, N, used were $2, 4, 8, 16, 32$. Each slab was then uniformly refined into rectangular space-time elements of unit aspect ratio. The vertical axis represents the energy norm of the error at the terminal time $t = 1$, while the horizontal axis denotes the reciprocal of the element diameters $1/h$.

4.2.1. Rectangular channel problem

The first problem considered here involves two-dimensional propagation of nonlinear thermal waves generated by a pulsing laser heat source in a regular domain. The rectangular channel domain, as depicted in Figure 5(a), occupies the planar region $\Omega = [0,\ 2] \times [-0.5,\ 0.5]$. The laser pulse incident on the left of the domain is represented as a Gaussian-type heat source given by

$$Q(x, y, t) = \frac{1}{2Dt_p} \exp\left[-\left(\frac{1+x}{D}\right)^2 - \left(\frac{y}{\Delta_r}\right)^2 - \left(\frac{t}{t_p}\right)^2 \right], \tag{33}$$

where D is the penetration depth in the horizontal direction, Δ_r is the width of the pulse (the radius in the vertical direction), and t_p is the characteristic duration of the laser pulse. In the analysis, the values of the parameters used are $D = 0.05$, $\Delta_r = 0.10$, and $t_p = 0.10$.

The results presented here consider two models of thermal transmission. The first, type II thermal conduction, corresponds to $k_1 = 1$ and $k_2 = 0$, while the other, type III thermal

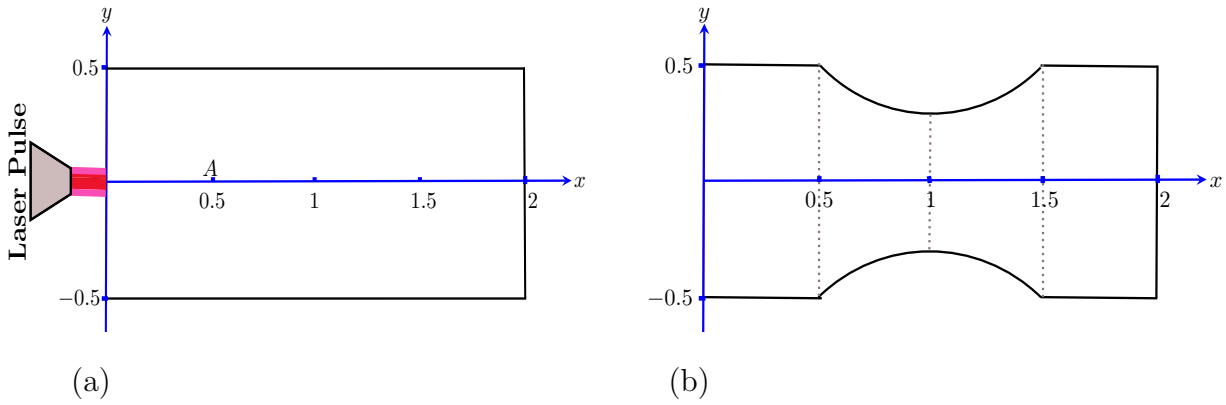

Figure 5: Pulsing laser study: schematic of two-dimensional domains of a rectangular (a) and a converging-diverging (b) channel.

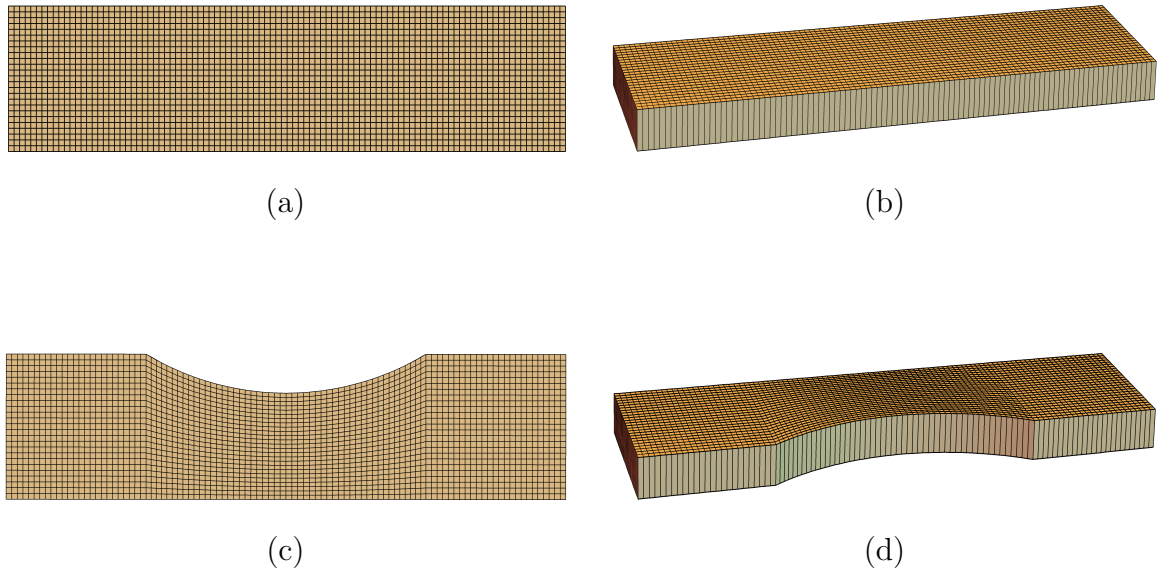

Figure 6: Spatial, (a) and (c), and space-time, (b) and (d), meshes of the computational domains of rectangular, (a) and (b), and converging-diverging, (c) and (d), channels. Note that the actual spatial mesh density used in the simulation was higher than displayed here, and the temporal duration Δt is magnified for viewing.

conduction mode, corresponds to $k_1 = 0.5$ and $k_2 = 0.2$. A situation is chosen in which the system is driven by the pulsing laser heat source only, that is, the initial conditions with respect to α and ϑ are chosen to be homogeneous. Moreover, the boundaries of the channel in each case are assumed to be insulated throughout the simulation.

We exploit the symmetry of the problem by taking as the analysis domain the upper-half of Ω, that is, $[0,\ 2] \times [0,\ 0.5]$. For the simulation, we used 100×50 quadrilateral elements spatially as shown in Figure 6(a). In the temporal direction each space-time slab consists of one element of thickness $\Delta t = 0.01$, resulting in 100×50 trilinear space-time elements, in which the space-time mesh shown in Figure 6(b) are used at each time step.

Figure 7 shows a time sequence of snapshots of the evolution of temperature distribution, according to type II (left) and type III (right) models of heat conduction, within the rectangular channel domain Ω. The numerical solutions obtained from the simulations using the TDG FE scheme are reflected about the x-axis in the visualization to give the complete problem domain. At $t = 0.10$ it is shown that the Gaussian-type laser pulse generates a thermal distribution whose shape reflects its source with a somewhat sharper front. The wave reaches the boundary at $t = 0.50$ and is reflected back into the channel. At $t = 1.00$ the reflected thermal waves are seen to interact nonlinearly, resulting in a nearly uniform temperature distribution in the region between their peaks, while the non-reflected part of the wave is at about halfway into the channel. Finally, at $t = 2.00$ the wave reaches the other end of the channel and reflects backwards. The other important nonlinear feature of the thermal wave is demonstrated through its appearance. As the wave propagates forward its front gets sharper and it also appears to be extended from behind, the well-known nonlinear feature referred to as *rarefaction*. On the other hand the plots to the right of Figure 7 show the thermal energy transmission in the type III model. It is shown in these plots that the wave mechanism of thermal energy still exists in this case with more attenuation.

Figure 8(a) presents the temperature profile along the mid-line $y = 0$ at time $t = 0.6$. The temperature curve corresponding to the classical theory, type I, is superimposed to serve as a reference for the non-classical models. It is noted that the peaks of both curves corresponding to type II and III have been shifted to the right compared to the one with

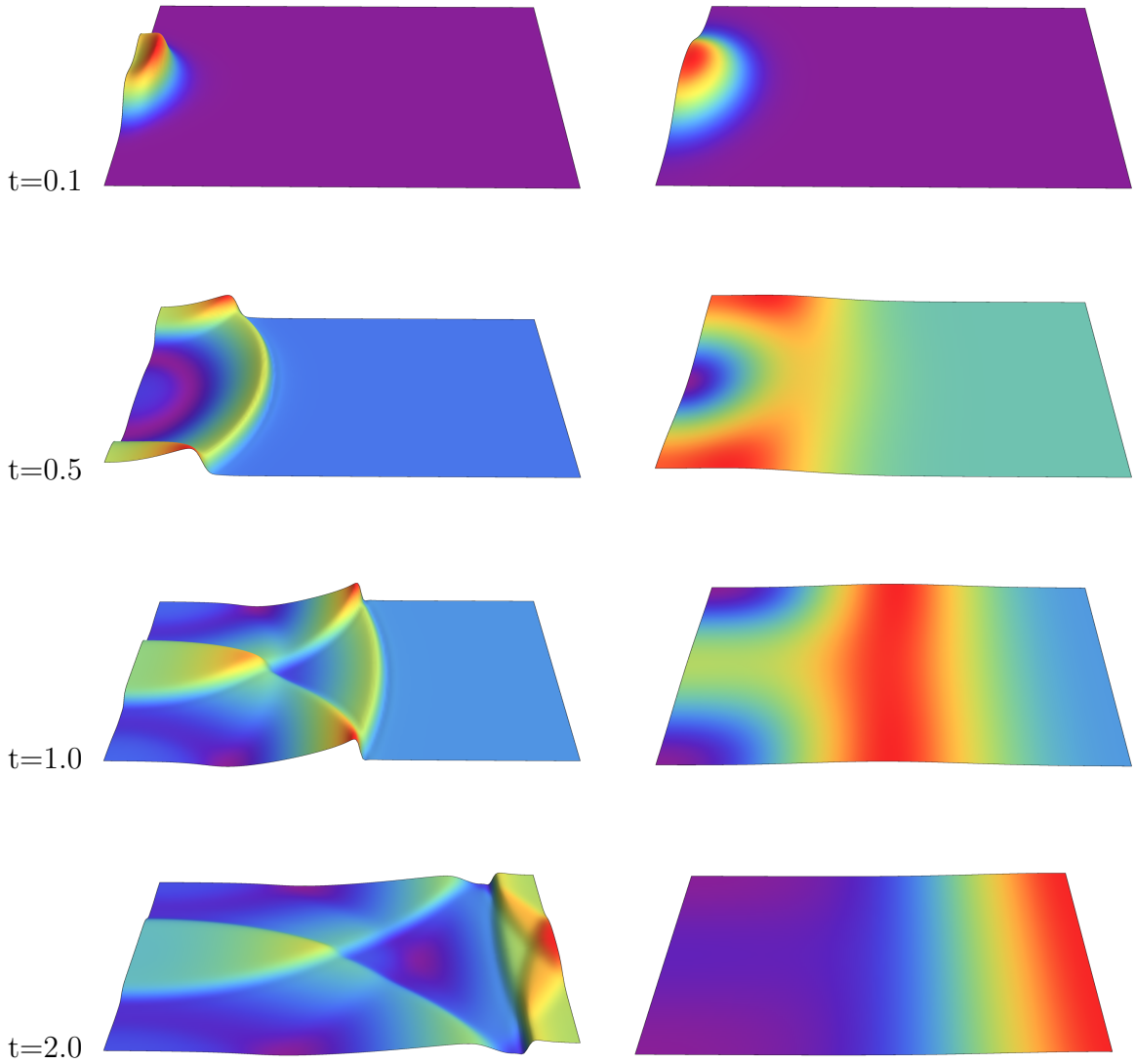

Figure 7: Temperature evolution, according to type II (left column) and type III (right column) non-classical heat conduction, in the rectangular channel domain heated by a Gaussian-type laser pulse

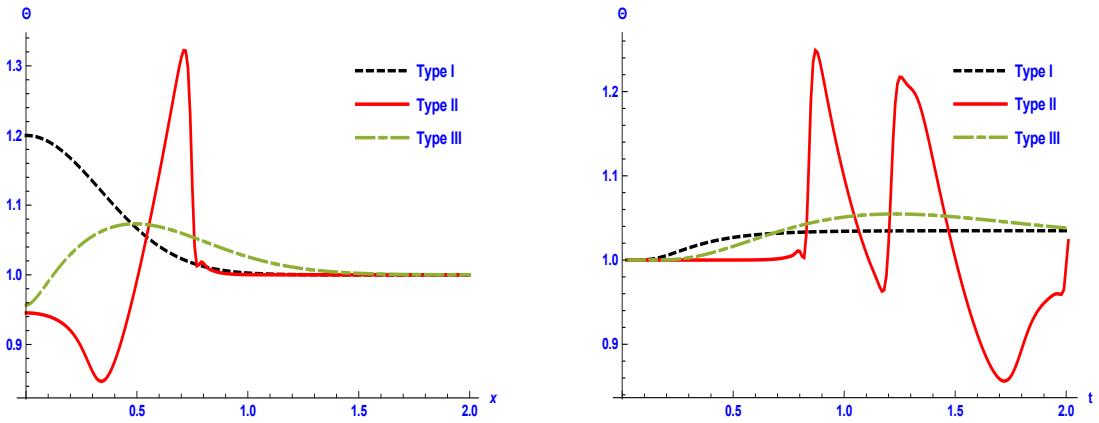

(a) (b)

Figure 8: Temperature profiles according to the various heat conduction models in the rectangular channel domain (a) across the mid-horizontal axis $y = 0$ at time $t = 0.6$, and (b) at the point $A(0.5,\ 0)$ over the duration $t \in [0,\ 2]$

type I. This is an indication that both type II and III support wave propagation of thermal energy. We also notice that the peak of the type II curve is accompanied by a sharp front but this is not observed in the case of type III, for which case the dissipation is higher and the profile appears to be smoother. Apart from the small over- and under-shoot at the foot of the wave peak, the TDG FE scheme captures the sharp wavefront well. It generally resolves a number of fine scale solution features which are particularly important in the nonlinear dynamics of thermal waves. Figure 8(b) shows the temperature profile of a point in the channel domain at $(0.5,\ 0)$ over the whole duration of the simulation. In case of type II, it is clearly seen that the thermal disturbances reach the point at about $t = 0.8$. Later, the thermal waves which were reflected by the boundary reach the point at about $t = 1.3$. In the case of type I, it is clearly shown that the temperature increases almost immediately after the laser pulse is applied, which demonstrates the fact that Fourier's or type I heat conduction permits an instantaneous transmission of thermal energy. The temperature profile of type III is characterized by its dissipative feature and wave mechanism of transmission of thermal energy. Unlike the case of type I, the temperature rise does not happen immediately after the thermal disturbance that has been induced in the form of the pulsing laser heat source.

4.3. Converging-diverging channel problem

The objective of this problem is to demonstrate the ability of the TDG FE method to model and capture complex solution features of heat conduction problems involving thermal wave propagation through a more complicated region. As shown in Figure 5(b), the domain consists of a uniform inlet followed by a converging-diverging region, and then a uniform outlet. This problem has also been investigated in [21] with the linear hyperbolic heat conduction model of Cattaneo-Vernotte-Maxwell. A pulsing laser modelled as a Gaussian-type heat source Q given by equation (33) is applied to the left of the channel domain. The pulse is of $D = 0.05$ penetration depth, $\Delta_r = 0.10$ width, and $t_p = 0.10$ characteristic duration.

Two cases are considered: the first, type II, corresponds to $k_1 = 1$ and $k_2 = 0$, and the second, type III, corresponds to $k_1 = 0.5$, and $k_2 = 0.2$. Homogeneous initial conditions with respect to α and ϑ are considered, and the boundaries of the domain are insulated throughout the simulation.

The problem is symmetrical with respect to the x-axis, and only the upper-half of the domain is analyzed. An optimal spatial mesh, as shown in Figure 6(c), with each element having aspect ratio as close to one as possible is considered, and consists of 115×50 quadrilateral elements. In the temporal direction each space-time slab is of single layer, $N = 1$, with duration $\Delta t = 0.01$. In total 115×50 trilinear space-time elements were used for each space-time slab. In the visualization, the numerical solution obtained from the simulations using the fully-time-discontinuous Galerkin method are reflected about the x-axis to give the complete problem domain. The images shown in Figure 9 are 3D scatter plots such that for each node within the domain a point is shown with its color and height corresponding to the temperature at that point.

Figure 9 shows the temporal sequence of the evolution of temperature according to the nonlinear heat conduction models. The plots at the right side of Figure 9 show the evolution of temperature according to the type II model. The plot at $t = 0.1$ shows the early stages of the temperature distribution reflecting the Gaussian-type thermal pulse with a sharper front. At $t = 0.5$ the wave is about to enter the converging region, while some boundary interaction patterns are also evident. As the wave passes through the compression region, it is expected that the amplitude of the waves will increase. This results in a layered thermal distribution as shown at $t = 2$, created by the waves reflected by the boundaries. This pattern is clearly different from the one obtained for the regular channel domain shown in Figure 7. On the other hand, the thermal distribution patterns according to the type III model do not seem to be affected by the complexity of the geometry, and are similar to those obtained for the regular channel domain.

5. Conclusion and discussion

In this paper, we have presented an overview the generalized thermal conduction model and showed its nonlinear stability which is embodied by its thermodynamic consistency. Two numerical methods based on the framework of space-time Galerkin methods for the numerical implementation of the generalized model have been formulated and discussed. The numerical stability of the TDG and cG FE schemes have been proved using the energy method which imitates the dissipative property of the continuous model. Numerically we have demonstrated that the TDG FE has better stability and accuracy features. The numerical result has also indicated that the accuracy of the TDG scheme does not depend on N. Moreover, the numerical simulation of the thermal response of a rigid material under short pulsed laser heating has been modeled using the TDG FE method. These simulations have shown that performance and capability of the TDG FE scheme in representing fine solution features.

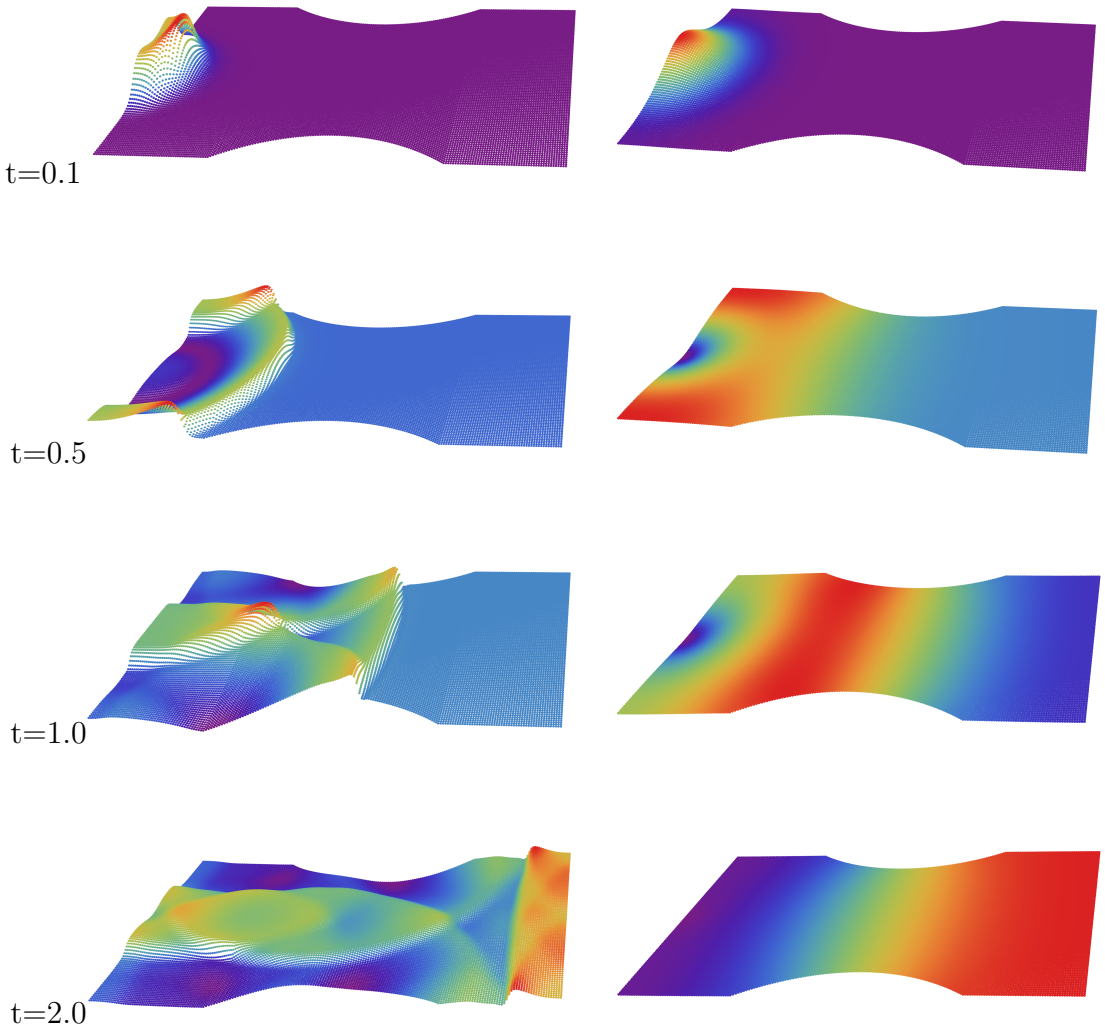

Figure 9: Temperature evolution, according to type II (Left) and type III (right) theory of non-classical theory of nonlinear heat conduction, in the converging-diverging channel domain heated by a Gaussian-type laser pulse

Acknowledgments

The work reported in this paper has been supported by the National Research Foundation of South Africa through the South African Research Chair in Computational Mechanics. This support is acknowledged with thanks.

References

[1] X. Ai, B. Q. Li, Numerical simulation of thermal wave propagation during laser processing of thin films, J. Electron. Mater. 34(5) (2005) 583–591. J.

[2] S. Bargmann, A. Favata, Continuum mechanical modeling of laser-pulsed heating in polycrystals: A multi-physics problem of coupling diffusion, mechanics, and thermal waves, ZAMM Zeitschrift fur Angew. Math. und Mech. 94 (2014) 487–489.

[3] M. J. Fryer, H. Struchtrup, Moment model and boundary conditions for energy transport in the phonon gas, Contin. Mech. Thermodyn. (2013) 1–26.

[4] W. Nernst, Die theoretischen und experimentellen grundlagen des neuen Wärmesatzes, Halle 35 (1918).

[5] L. Tisza, Sur la supraconductibilité thérmique de l'helium II liquide et la statistique de Bose-Einstein, C.R. Acad. Sci. 35 (1938) 1035.

[6] L. Landau, Theory of the superfluidity of Helium II, Phys. Rev. 60(4) (1941) 365–358.

[7] R. J. Donnelly, The two-fluid theory and second sound in liquid helium, Phys. Today 62(10) (2009) 34–39.

[8] R. J. Donnelly, The second sound in Helium II, J. Phys. 8 (1944) 381.

[9] C. C. Ackerman, B. Bertman, H. A. Fairbank, R. A. Guyer, Second sound in solid helium, Phys. Rev. Lett. 16(18) (1966) 789.

[10] C. C. Ackerman, W. C. O. Jr., Second sound in solid helium-3, Phys. Rev. Lett., 22(15) (1969) 764.

[11] H. E. Jackson, C. T. Walker, T. F. McNelly, Second sound in NaF, Phys. Rev. Lett. 25(1) (1970) 26.

[12] V. Narayanamurti, R. C. Dynes, Observation of second sound in bismuth, Phys. Rev. Lett. 28(22) (1972) 1461.

[13] P. Ván, Theories and heat pulse experiments of non-Fourier heat conduction, Commun. Appl. Ind. Math., 7(2) (2016) 150–166.

[14] K. Tamma, X. Zhou, Macroscale and microscale thermal transport and thermo-mechanical interactions: Some noteworthy perspectives, J. Therm. Stress., 21(3) (1988) 405–449.

[15] D. S. Chandrasekharaiah, Hyperbolic thermoelasticity: A review of recent literature, Appl. Mech. Rev. 51 (1998) 705–729.

[16] D. D. Joseph, L. Preziosi, Heat waves, Rev. Mod. Phys. 61(1) (1989) 41–73. .

[17] D. Joseph, L. Preziosi, Addendum to the paper 'Heat waves', Rev. Mod. Phys. 6(2) (1990) 375–391.

[18] C. Cattaneo, Sur une forme de l'équation de la chaleur éliminant le paradoxe d'une propagation instantanée, Comptes Rendus, 247(4) (1958) 431.

[19] P. Vernotte, Les paradoxes de la théorie continue de l'équation de la chaleur, C.R. Acad. Sci. 246 (1958) 3154–3155.

[20] J. C. Maxwell, On the dynamical theory of gases, Philos. Trans. Roy. Soc. 157 (1867) 49–88.

[21] S. T. Miller, R. B. Haber, A space-time discontinuous Galerkin method for hyperbolic heat conduction, Comput. Methods Appl. Mech. Eng. 198(2) (2008) 194–209.

[22] D. Y. Tzou, Experimental support for the lagging behavior in heat propagation, J. Thermophys. Heat Transf. 9(4) (1995) 686–693.

[23] D. S. Chandrasekharaiah, Thermoelasticity with second sound: A Review, Appl. Mech. Rev. 39(3) (1996) 355.

[24] R. B. Hetnarski, J. Ignacza, Generalized thermoelasticity, J. Therm. Stress. 22(4–5) (1999) 451–476.

[25] F. F. Wang, B. Wang, Current research progress in non-classical Fourier heat conduction, Appl. Mech. Mater. 442 (2014) 187–196.

[26] D. M. Chang, B. L. Wang, Transient thermal fracture and crack growth behavior in brittle media based on non-Fourier heat conduction, Eng. Fract. Mech. 94 (2012) 29–36.

[27] K. C. Liu, P. J. Cheng, J. S. Wang, Analysis of Thermal Damage in a Laser-irradiated Based on the non-Fourier Model, Int. J. Eng. Technol. 6(2) (2014) 132–135, .

[28] K. C. Liu, J. C. Wang, Analysis of thermal damage to laser irradiated tissue based on the dual-phase-lag model, Int. J. Heat Mass Transf. 70 (2014) 621–628.

[29] R. Shirmohammadi, Thermal response of microparticles due to laser pulse heating, Nanoscale Microscale Thermophys. Eng. 15(3) (2011) 151–164.

[30] T. J. Bright, Z. M. Zhang, Common misperceptions of the hyperbolic heat equation, J. Thermophys. heat Transf. 23(3) (2009) 601–607.

[31] F. EKoue, A. F. d'Halloy, D. Gigon, G. Plantamp, E. Zajdman, Maxwell-Cattaneo regularization of heat equation, Int. Sch. Sci. Res. Innov. 7(5) (2013) 772–775.

[32] Y. J. Yu, C. L. Li, Z. N. Xue, X. G. Tian, The dilemma of hyperbolic heat conduction and its settlement by incorporating spatially nonlocal effect at nanoscale, Phys. Lett. Sect. A Gen. At. Solid State Phys. 380(1-2) (2016) 255–261.

[33] R. Kovács, P. Ván, Generalized heat conduction in heat pulse experiments, Int. J. Heat Mass Transf. 83 (2015) 613–620.

[34] M. F. Wakeni, B. D. Reddy, A. T. McBride, A thermodynamically consistent formulation of generalized thermoelasticity at finite deformations, Int. J. Eng. Sci. 108 (2016) 1–8.

[35] A. E. Green, P. M. Naghdi, A re-examination of the postulates of thermomechanics, Proc. R. Soc. London Ser. A 423 (1991) 171–194.

[36] A. E. Green, P. M. Naghdi, On undamped heat waves in an elastic solid, J. Therm. Stress. 15 (1992) 253–264.

[37] A. E. Green, P. M. Naghdi, Thermoelasticity without energy dissipation, J. Elast. 31 (1993) 189–208.

[38] A. E. Green, P. M. Naghdi, A new thermoviscous theory of fluids, J. Nonnewton. Fluid Mech. 56 (1995) 289–306.

[39] A. E. Green, P. M. Naghdi, A unified procedure for construction of theories of deformable media. I. Generalized continua, Proc. R. Soc. London Ser. A 448 (1995) 335–356.

[40] P. M. Jordan, B. Straughan, "Acoustic acceleration waves in homentropic Green and Naghdi gases," Proc. R. Soc. A Math. Phys. Eng. Sci. 462(2076) (2006) 3601–3611.

[41] S. Bargmann, P. Steinmann, P. M. Jordan, On the propagation of second-sound in linear and nonlinear media: Results from Green-Naghdi theory, Phys. Lett. Sect. A Gen. At. Solid State Phys. 372(24) (2008) 4418–4424.

[42] S. Bargmann, Remarks on the Green-Naghdi theory of heat conduction, J. Non-Equilibrium Thermodyn. 38(2) 101–118.

[43] C. Giorgi, D. Grandi, V. Pata, On the green-naghdi type iii heat conduction model, Discret. Contin. Dyn. Syst. Ser. B 19(7) (2014) 2133–2143.

[44] M. C. Leseduarte, R. Quintanilla, On uniqueness and continuous dependence in type III thermoelasticity, J. Math. Anal. Appl. 395(1) (2012) 429–436.

[45] A. Sasmal, S. C. Mishra, Analysis of non-Fourier conduction and radiation in a differentially heated 2-D square cavity, Int. J. Heat Mass Transf. 79 (2014) 116–125.

[46] S. C. Mishra, H. Sahai, Analyses of non-Fourier heat conduction in 1-D cylindrical and spherical geometry – An application of the lattice Boltzmann method, Int. J. Heat Mass Transf. 55(23-24) (2012) 7015–7023.

[47] H. Zhang, S. Zhang, X. Guo, J. Bi, Multiple spatial and temporal scales method for numerical simulation of non-classical heat conduction problems: One dimensional case, Int. J. Solids Struct. 42(3-4) (2005) 877–899.

[48] B. L. Wang, J. C. Han, Y. G. Sun, A finite element/finite difference scheme for the non-classical heat conduction and associated thermal stresses, Finite Elem. Anal. Des. 50 (2012) 201–206.

[49] S. Bargmann, P. Steinmann, Theoretical and computational aspects of non-classical thermoelasticity, Comput. Methods Appl. Mech. Eng. 196(1-3) (2006) 516–527.

[50] S. Bargmann, P. Steinmann, Modeling and simulation of first and second sound in solids, Int. J. Solids Struct. 45(24) (2008) 6067–6073.

[51] M. F. Wakeni, B. D. Reddy, A. T. McBride, An unconditionally stable algorithm for generalized thermoelasticity based on operator-splitting and time-discontinuous Galerkin finite element methods, Comput. Methods Appl. Mech. Eng. 306 (2016) 425–451.

[52] C. Johnson, Discontinuous Galerkin finite element methods for second-order hyperbolic problems, Comput. Methods Appl. Mech. Eng. 107(1-2) (1993) 117–129.

[53] D. K. Khalmonova, F. Costanzo, A space-time discontinuous Galerkin finite element method for fully coupled linear thermo-elasto-dynamic problems with strain and heat flux discontinuities, Comput. Methods Appl. Mech. Eng. 197(13-16) (2008) 1323–1342.

[54] F. Costanzo, H. Huang, Proof of unconditional stability for a single-field discontinuous Galerkin finite element formulation for linear elasto-dynamics, Comput. Methods Appl. Mech. Eng. 194(18-20) (2005) 2059–2076.

[55] G. M. Hulbert, T. J. R. Hughes, Space-time finite element methods for second-order hyperbolic equations, Comput. Methods Appl. Mech. Eng. 84 (1990) 327–348.

[56] T. J. R. Hughes, G. M. Hulbert, Space-time finite element methods for elastodynamics: Formulations and error estimates, Comput. Methods Appl. Mech. Eng. 66(3) (1988) 339–363.

[57] S. T. Miller, B. Kraczek, R. B. Haber, D. D. Johnson, Multi-field space-time discontinuous Galerkin methods for linearized elastodynamics, Comput. Methods Appl. Mech. Eng. 199(1-4) (2009) 34–47.

[58] R. Abedi, R. B. Haber, S. Thite, An h-adaptive space-time-discontinuous Galerkin method for linearized elastodynamics, Eur. J. Comput. Mech. 15(6) (2006) 619–642.

[59] R. Abedi, B. Petracovici, R. B. Haber, A space-time discontinuous Galerkin method for linearized elastodynamics with element-wise momentum balance, Comput. Methods Appl. Mech. Eng. 195(25-28) (2006) 3247–3273.

[60] R. Abedi, R. B. Haber, Riemann solutions and space-time discontinuous Galerkin method for linear elastodynamic contact, Comput. Methods Appl. Mech. Eng. 270 (2014) 150–177.

[61] J. Korelc, Multi-language and multi-environment generation of nonlinear finite element codes, Eng. Comput. 18(4) (2002) 312–327.

[62] O. Schilling, X. Zhang, O. Bossen, Heat flowing from cold to hot without external intervention by using a “thermal inductor”, Sci. Adv. 5(4) (2009) 1–7.

[63] S. Huberman, R. Duncan, K. Chen, B. Song, V. Chiloyan, Z. Ding, A. A. Maznev, G. Chen, K. A. Nelson, Obsevation of second sound in graphite at temperatures above 100 K, Science 364(6438) (2019) 375–379.